

Radiative Invigoration of Tropical Convection by Preceding Cirrus Clouds

HIROHIKO MASUNAGA

Institute for Space-Earth Environmental Research, Nagoya University, Nagoya, Japan

SANDRINE BONY

LMD/IPSL, CNRS, Sorbonne Universities, University Pierre and Marie Curie, Paris, France

(Manuscript received 23 November 2017, in final form 12 February 2018)


ABSTRACT

This work seeks evidence for convective–radiative interactions in satellite measurements, with a focus on the variability over the life cycle of tropical convection in search of the underlying processes at a fundamental level of the convective dynamics. To this end, the vertical profiles of cloud cover and radiative heating from the *CloudSat*–*CALIPSO* products are sorted into a composite time series around the hour of convective occurrence identified by the TRMM PR. The findings are summarized as follows. Cirrus cloud cover begins to increase, accompanied by a notable reduction of longwave cooling, in moist atmospheres even 1–2 days before deep convection is invigorated. In contrast, longwave cooling stays efficient and clouds remain shallow where the ambient air is very dry. To separate the radiative effects by the preceding cirrus clouds on convection from the direct effects of moisture, the observations with enhanced cirrus cover are isolated from those with suppressed cirrus under a moisture environment being nearly equal. It is found that rain rate is distinctly higher if the upper troposphere is cloudier regardless of moisture, suggesting that the cirrus radiative effects may be linked with the subsequent growth of convection. A possible mechanism to support this observational implication is discussed using a simple conceptual model. The model suggests that the preceding cirrus clouds could radiatively promote the moistening with the aid of the congestus-mode dynamics within a short period of time (about 2 days) as observed.

1. Introduction

The latent heat released by vapor condensation is the primary heat source being balanced against the net radiative cooling in the global atmospheric energy budget (Trenberth et al. 2009; L'Ecuyer et al. 2015), underscoring the central importance of moist convection and radiative processes, and in particular the mechanism underlying their coupling. Perturbations to the cloud and moisture fields brought by moist convection radiatively modify its ambient thermodynamics, which has the potential to promote or suppress the convective activity in return. Such a radiative–convective feedback is arguably at work in aspects of the global or tropical climate (e.g., Wetherald and Manabe 1988; Randall

et al. 1989; Ramanathan and Collins 1991; Tompkins and Craig 1998; Raymond 2000; Lindzen et al. 2001; Hartmann and Larson 2002; Stephens et al. 2008; Bony et al. 2016) and in its internal variability such as the intraseasonal oscillations (e.g., Hu and Randall 1994; Raymond 2001; Lee et al. 2001; Sobel and Gildor 2003; Lin et al. 2004; Bony and Emanuel 2005; Kim et al. 2015). Whereas specific details of the mechanism vary from one study to another, a radiative perturbation exerted by extensive anvil clouds is in general thought of as a critical ingredient of radiative–convective feedbacks. Water vapor and shallow clouds can be additional key players (Nilsson and Emanuel 1999; Fermepin and Bony 2014) and have drawn growing interest in the context of convective self-aggregation (Bretherton et al. 2005; Muller and Held 2012; Wing and Emanuel 2014; Coppin and Bony 2015).

 Denotes content that is immediately available upon publication as open access.

Corresponding author: Hirohiko Masunaga, masunaga@nagoya-u.jp



This article is licensed under a [Creative Commons Attribution 4.0 license](http://creativecommons.org/licenses/by/4.0/) (<http://creativecommons.org/licenses/by/4.0/>).

By contrast, much less attention has been paid to the role of radiation in exploration for the dynamics of individual convective systems. The radiative processes are conventionally considered not to substantially alter the structure and evolution of vigorous convective systems (Houze 2004) except perhaps as a driver of the diurnal modulation (Gray and Jacobson 1977; Xu and Randall 1995; Chen and Houze 1997), although some existing work reported discernible impacts by radiation (Webster and Stephens 1980; Houze 1982; Tao et al. 1996). One might rule out radiation by arguing that latent heating in deep convective clouds reaches $10\text{--}100\text{ K day}^{-1}$ or even more and hence overwhelms radiative cooling, which is typically $1\text{--}10\text{ K day}^{-1}$ in magnitude on an instantaneous basis. The radiative effects, however, prevail widely and persistently as opposed to the localized, sporadic nature of latent heating. The averaging over a large domain can dilute the predominance of latent heating over radiative cooling to the extent that, for instance, radiation can offset 20% of net condensation in the large-scale temperature budget (Tao et al. 2004; Li et al. 2013). The imbalance between the two would be further mediated when integrated over time, explaining partly why a radiative–convective feedback is identified always in the climatological or intraseasonal context in the literature above. The widely accepted perception that radiative processes vary slowly, however, is challenged by the observations showing a significant day-to-day variability in radiative heating (Ciesielski et al. 2003), raising the question of whether radiation can influence tropical meteorology on short time scales as well. Recalling that the lifetime of individual convective systems does not far exceed 0.5–1 day even for a long-lived organized system (Chen and Houze 1997), it is unclear yet whether a salient radiative–convective feedback emerges only as the result of low-pass spatial–temporal filtering, or is somehow intrinsic to a more fundamental level of the convective dynamics as well. This study is motivated to explore this latter possibility, which appears to have been practically ignored in a large body of past work.

In the current analysis, the evolution of the cloud structure and the associated radiative field over the passage of tropical disturbances are investigated using satellite observations. To put discrete satellite snapshots into the evolutionary context, the *CloudSat* and *CALIPSO* measurements are sorted into a statistical time series on a subdaily to a multiple-day time scale, using the TRMM PR detection of precipitation as an anchor for constructing the composite time sequence. A more thorough description of the data and analysis scheme is provided in section 2. Section 3 presents the analysis results, followed by an attempt to discuss the implications based on a simple conceptual model in section 4. The findings are concluded in section 5.

2. Data and method

The satellite datasets and analysis method are described in this section.

a. Satellite data

The *CloudSat* and *CALIPSO* satellites, launched in April 2006, fly in formation as a part of the A-Train constellation and have sun-synchronous overpasses fixed approximately at 0130 and 1330 local time (LT) at any location that the satellites fly over. The *CloudSat* carries a W-band (94 GHz) cloud-profiling radar capable of measuring a broad spectrum of clouds from cumulonimbus to cirrus, with the caveat that optically thin cirrus clouds that cover 30% of the tropics are left undetected (Haladay and Stephens 2009). The CALIOP, a dual-wavelength lidar aboard the *CALIPSO*, complements *CloudSat* observations owing to its high sensitivity to thin cirrus clouds at the expense of severe attenuation within modest to thick cloud layers. This work adopts the merged *CloudSat* and *CALIPSO* (2B-GEOPROF-lidar) Release 4 (R04) product (Mace et al. 2009) to analyze the vertical structure of cloud cover. The vertical profiles of radiative heating rate Q_R are obtained also from the combined radar–lidar product or 2B-FLXHR-lidar R04 dataset (L'Ecuyer et al. 2008; Henderson et al. 2013). This product provides the estimates of longwave (LW) and shortwave (SW) Q_R by applying radiative transfer calculations to the observed cloud properties and the collocated ECMWF analysis of air temperature and humidity.

The occurrence of precipitation is determined by the TRMM PR whenever the radar echo exceeds 19 dBZ across three or more consecutive range bins at any height in the column. This number is chosen to be slightly higher than the nominal value of the minimum detectable level or 17 dBZ (Kummerow et al. 1998) because the PR sensitivity has been slightly reduced since the TRMM orbital boost in August 2001. The TRMM 2A25 version 6 product is analyzed here, while the PR calibration has been quite stable and is virtually unaffected by the product version in use. Column water vapor (CWV) estimates from the TRMM TMI are obtained from the Remote Sensing Systems (RSS) version 7 daily (i.e., instantaneous) product. The PR precipitation and TMI CWV are by design sampled on a simultaneous basis. In addition, the *Aqua* AMSR-E estimates of SST, CWV, and precipitation are employed from the RSS version 7 daily product. The AMSR-E instrument, as a member of the A-Train constellation, provides synchronized observations with *CloudSat* and *CALIPSO* measurements. To avoid confusion, CWV obtained from the TMI is hereinafter denoted by CWV_0 , as it serves as the value at the origin on the composite

time axis (see section 2b). CWV without any subscript refers to the AMSR-E estimates.

The present analysis is targeted on the 3.5-yr period from 1 July 2006 to 31 December 2009 over global tropical oceans bound between 20°S and 20°N with all islands masked out.

b. Analysis method

Low-Earth-orbiting (LEO) satellites such as the *CloudSat* and *CALIPSO* fly over a given location only sporadically, so the observations from those satellites do not constitute a continuous time sequence delineating the evolution of individual cloud systems. A series of previous work initiated by Masunaga (2012, 2013) devised a method to statistically reconstruct the temporal evolution of convective systems from intermittent LEO satellite observations. The current analysis strategy is based on this methodology as outlined below. First, *CloudSat*–*CALIPSO* snapshots are collected every time when a precipitation event is spotted by the TRMM PR some hours before or after at a same location. The *CloudSat*–*CALIPSO* measurements within the distance of 100 km from the PR-detected precipitation are included in the analysis so that the resulting statistics represent the large-scale mean field with a horizontal scale of $O(100)$ km. Each snapshot is then projected onto a time axis with respect to the temporal difference between the *CloudSat*–*CALIPSO* and TRMM observations, with the TRMM being always assigned onto time zero. For example, a column of *CloudSat*–*CALIPSO* measurements is time stamped as -3 h if observed earlier by 3 h than the TRMM measurements. The time difference between the satellites varies from one orbit to another, as the local time of sun-asynchronous TRMM overpasses drifts over time. Once this procedure is completed for all the data to be analyzed, the *CloudSat*–*CALIPSO* snapshots are averaged within each hourly bin along the time axis to yield the composite time series of cloud properties. Although the composite base point ($t = 0$) is not designed to single out a specific stage of convective evolution, it turns out that the life cycle of convection naturally emerges itself in the composite time series. The analysis results are presented in the following section.

3. Composite time series

a. The vertical structure of cloud cover

The general aspects of the composite cloud properties are first examined. Throughout this work, the satellite measurements are analyzed separately for dry and moist atmospheres since the magnitude and vertical structure

of radiative heating vary substantially with the moisture environment. This is done by stratifying the composite time series by the CWV measured at time zero (CWV_0). The ambient humidity is classified here by three CWV classes: dry ($CWV_0 \leq 35$ mm), moderate ($35 < CWV_0 \leq 50$ mm), and moist ($CWV_0 > 50$ mm). The composite time series is composed of $\sim 2 \times 10^4$ *CloudSat*–*CALIPSO* samples at each hour for the dry class, $\sim 7 \times 10^4$ for the moderate, and $\sim 4 \times 10^5$ for the moist.

Figure 1 shows the composite time series of *CloudSat*–*CALIPSO* cloud cover for the three moisture classes. The contrast is striking across different moisture environments. The dry case (Fig. 1, top panel) is virtually cloud-free above the boundary layer (or the layer between 0 and 2 km). Shallow clouds confined in the boundary layer prevail at all times, with a clear sign of diurnal cycle that is aliased into the time series. Cloud cover somewhat enhances above 2 km, particularly near the tropopause in the moderately humid atmosphere (middle). The moist environment (bottom) allows vigorous cloud systems to develop around time zero as signified by a rapid growth of cloud cover to beyond 0.4 in the whole thickness of the troposphere. Given that the composite field is defined for a large-scale (~ 100 km) domain, a cloud cover exceeding 0.4 suggests a substantial population of cumulonimbus towers and/or stratiform cloud anvils and hence the occurrence of organized convective systems.

The moist case also exhibits a few other notable features. Cirrus clouds prevail even during a convectively inactive period away from time zero. Cirrus cloud cover stays persistently near 0.4 and is further enhanced to beyond 0.5 during 1–2 days prior and subsequent to $t = 0$. The boundary layer (less than ~ 2 km in height) is initially not as cloudy as the upper troposphere, but is increasingly populated with shallow clouds over hours prior to the peak convection in parallel with the cirrus enhancement. On the other hand, midtropospheric cloudiness does not rise until $t = -12$ h and decays quickly after $t = 12$ h. Interestingly, midtropospheric cloudiness is slightly larger above ~ 5 km than immediately below, resulting in a modest vertical discontinuity in between. Similar cloudiness profiles have been observed during past field campaigns over tropical ocean (Zuidema 1998; Yasunaga et al. 2006).

One would expect that cirrus cloud cover increases during and after the vigorous convection accompanied by extensive anvil cloud decks. Somewhat surprising, on the other hand, is the fact that cirrus cloud cover begins to flourish as early as $t = -24$ h, long before the convection intensifies into the penetrating cloud tower. The cirrus increase prior to the convection is a robust signal beyond the statistical error inherent in the composite

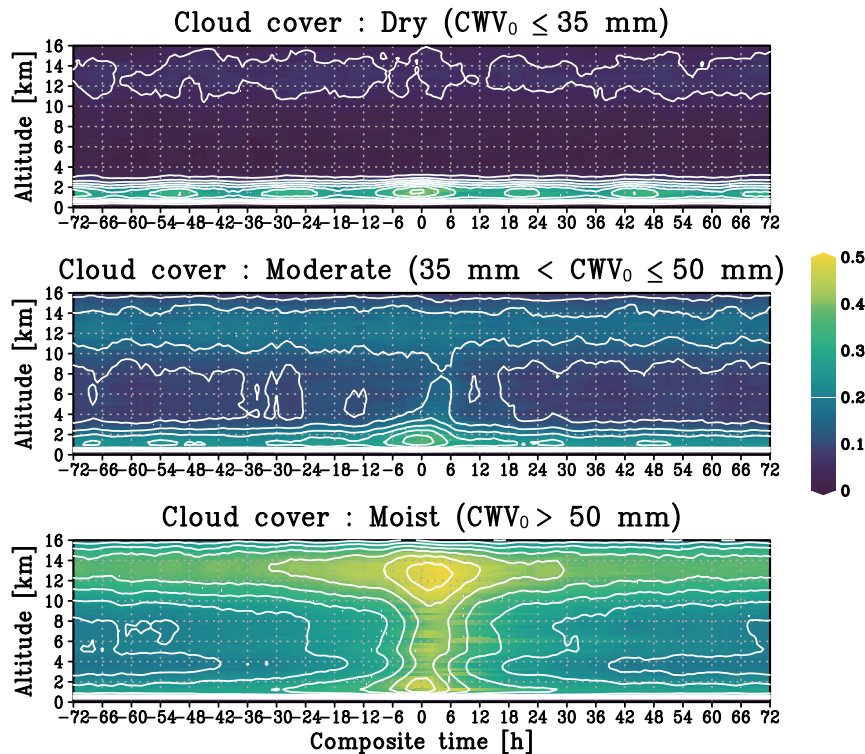


FIG. 1. The composite time series of *CloudSat*–*CALIPSO* cloud cover, color-shaded as indicated on the right and contoured every 0.05, for the (top) dry ($CWV_0 \leq 35$ mm), (middle) moderate ($35 < CWV_0 \leq 50$ mm), and (bottom) moist ($CWV_0 > 50$ mm) cases.

method, with the leading cirrus being even greater in cloud cover than the trailing cirrus (see [appendix](#)). The possible radiative effects of those preceding cirrus clouds in various moisture environments are examined next.

b. Radiative heating and moisture environment

The radiative heating profiles are plotted in [Fig. 2](#). To first assess the LW effects separately from the SW, only the descending or midnight (0130 LT) section of *CloudSat*–*CALIPSO* orbits are included in the composite statistics shown here, setting aside the shortwave effects until [section 3d](#). As will become clearer later, the cloud radiative effects (CREs) on the atmosphere (i.e., the difference in the all-sky flux minus clear-sky flux between the top and bottom of the atmosphere) are a major factor responsible for striking features seen in [Fig. 2](#). When the atmosphere stays dry ([Fig. 2](#), top panel), a strong radiative cooling of $\sim -3 \text{ K day}^{-1}$ dominates the lower troposphere immediately above 2 km, ascribable to LW emissions from shallow cloud tops ([Fig. 1](#), top). In contrast, the LW cooling is largely reduced below 4 km in the moist environment ([Fig. 2](#), bottom), owing to the downward LW radiation from

clouds above, primarily from cirrus clouds, remotely influencing the lower troposphere. A band of suppressed cooling at 4 km arises presumably because the vertical minimum in cloud cover at this height (see [Fig. 1](#), bottom) locally stifles the LW emission. Another band of muted cooling just above the surface is likely brought about by downward emissions from shallow cloud base in addition to the far-reaching cirrus LW effect. As cloud cover drastically increases at all heights during the peak convection, the cloud greenhouse effect grows so strong that Q_R approaches 0 K day^{-1} below 2 km around $t = 0$.

To further look into the dependence of LW cooling on the ambient moisture, the composite evolutionary tracks are projected onto the $\langle Q_R \rangle$ – CWV plane, where $\langle Q_R \rangle$ denotes column radiative heating integrated from the surface to the top of the atmosphere ([Fig. 3](#)). The five trajectories represent different moisture environments composed of the three cases presented in [Figs. 1](#) and [2](#) and two additional analysis runs carried out with the intermediate ranks of moderately dry ($30 < CWV_0 \leq 40$ mm) and moderately moist ($40 < CWV_0 \leq 55$ mm). The clear-sky $\langle Q_R \rangle$ is plotted in grayscale in addition to the all-sky $\langle Q_R \rangle$ in color. The all-sky $\langle Q_R \rangle$ appears to systematically increase with the ambient moisture over a broad range of

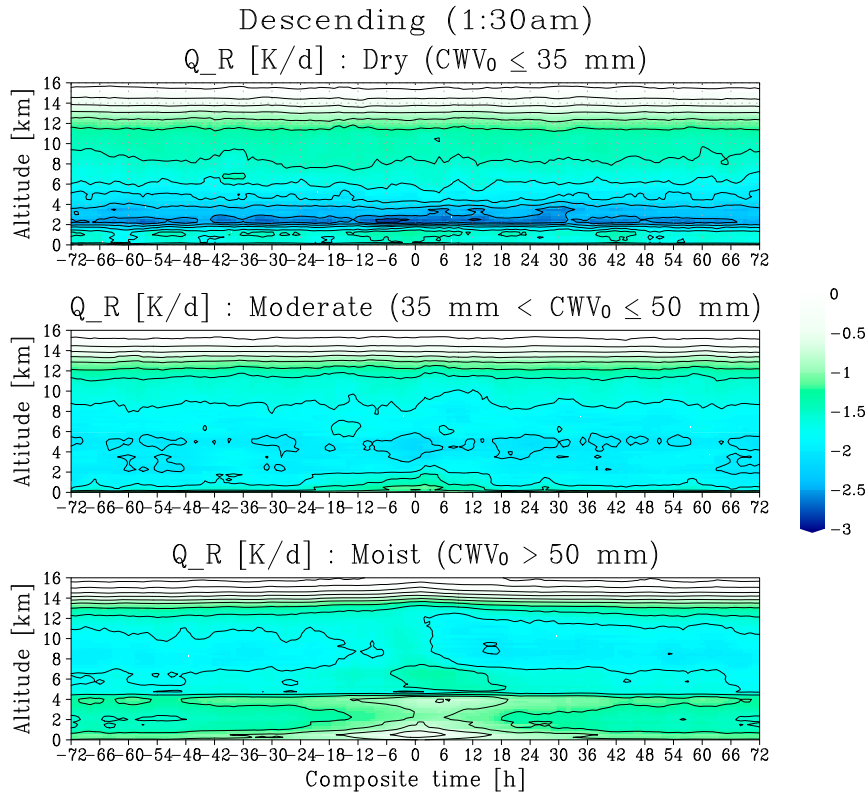


FIG. 2. As in Fig. 1, but for radiative heating rate Q_R (K day^{-1}) with descending (0130 LT) *CloudSat*–*CALIPSO* orbits only. The contour interval is 0.25 K day^{-1} .

CWV, while the clear-sky $\langle Q_R \rangle$ is significantly less sensitive to CWV. It follows that clouds, rather than water vapor, largely dominate the dependence of LW cooling on CWV, suggestive of a tight coupling between the cloud properties (coverage, thickness, top height, etc.) and the ambient moisture. The cloud radiative effect, or the all-sky $\langle Q_R \rangle$ minus clear-sky $\langle Q_R \rangle$, is found to be $+10$ – 20 W m^{-2} for CWVs of 40–45 mm and can be as large as $+60 \text{ W m}^{-2}$ when CWV is greater than 55 mm, indicating that the cloud greenhouse effect strengthens to a remarkable degree as the environment moistens.

Figure 3 also shows that the cloud LW effect is neutral around a CWV of 35 mm and is even slightly negative for lower CWV values. The LW radiation by shallow-cloud tops efficiently escapes to space when the free troposphere is very dry, as depicted by a sharp cooling peak around 2 km (Fig. 2, top), so an additional low-cloud cover enhances the LW emission out of the atmosphere.

c. Radiative impacts on convection

The sensitivity of tropical convection to free-tropospheric moisture has been well known from observations (e.g., Numaguti et al. 1995; Yoneyama and Fujitani 1995; Brown and Zhang 1997; Sherwood 1999;

Jensen and Del Genio 2006), so it is no surprise that convection develops deeper in a moister atmosphere (Fig. 1). The suppression of convection in a dry environment may be ascribed to the direct effects of mid-tropospheric dry air including a buoyancy loss due to the

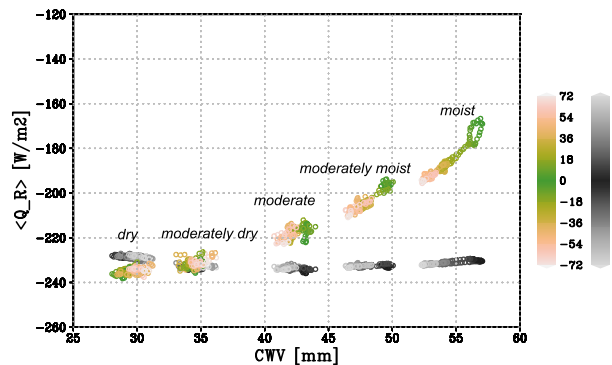


FIG. 3. The composite trajectory projected on the $\langle Q_R \rangle$ –CWV plane, constructed with descending (0130 LT) *CloudSat*–*CALIPSO* orbits only. Different trajectories are obtained for the five moisture setups as indicated for the all-sky $\langle Q_R \rangle$ in color and the clear-sky $\langle Q_R \rangle$ in gray. The color and gray scales designate the composite time (h) as shown on the right.

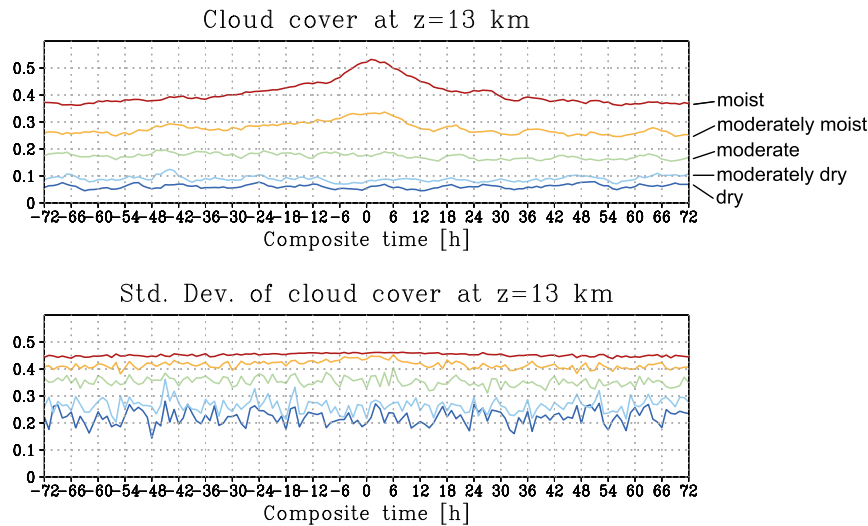


FIG. 4. The composite time series of (top) cirrus cloud cover and (bottom) its standard deviation at an altitude of 13 km for different moisture classes as indicated on the right. Both ascending and descending sections of *CloudSat*–*CALIPSO* orbits are included here because this cloud cover serves as the reference common to the midnight and afternoon composites.

entrainment and dry downdrafts into the subcloud layer. From the moist static energy (MSE) perspectives, on the other hand, column radiative heating is among the central players controlling the large-scale circulation involving moist convection (detailed discussion will be given in section 4a). It is difficult to separate the direct moisture effects from the radiative effects in the results presented so far.

Figure 4 shows the composite evolution of cloud cover at 13 km, a level selected to correspond roughly to the vertical maximum of cirrus cloud cover (Fig. 1, top panel). Repeating the same analysis with the mean upper-tropospheric cloud cover averaged between 10 and 15 km instead of the single layer at 13 km does not noticeably affect the results to follow (not shown). The standard deviation of cloud cover within the hourly samples (bottom) shows that the *CloudSat*–*CALIPSO* samples have considerable statistical spread around each composite curve, so the cloud radiative effect may actually be quite variable from one measurement to another even within a same CWV category. To partition the composite curves by $\langle Q_R \rangle$ with CWV being fixed as much as possible, another set of composite analysis runs are repeated but this time are broken down into two subsamples with high and low cirrus cloudiness, depending on whether cloud cover at 13 km is higher or lower than the original unconditional composite plotted in Fig. 4. In this way, the radiative effects by cirrus clouds are attempted to be isolated under a similar moisture environment. Note that the partitioning of cirrus cloudiness is applied to all *CloudSat*–*CALIPSO*

measurements at each hour along the composite time axis. As such, the strategy here is to delineate a contrast between two extreme cases having persistently high or low cirrus cloud cover, which are somewhat unrealistic but useful for testing the underlying physics. The implications for realistic applications will be discussed later in section 4.

Figure 5 illustrates the cirrus-rich and cirrus-poor cases separated as described above, together with the “control” case from Fig. 3 for comparison. As expected, LW cooling is suppressed (i.e., $\langle Q_R \rangle$ is less negative) in the cirrus-rich composites compared to the control, while enhanced in the cirrus-poor cases. The difference in $\langle Q_R \rangle$ increases with increasing CWV. Two pairs of contrasting cases are chosen to assess the possible roles of the cirrus radiative effects in different moisture environments: cases H1–L1 and H2–L2, as indicated in Fig. 5, that each span a common CWV range of approximately 45–50 mm and 50–55 mm, respectively. Here the prefixes H and L denote the cirrus-rich (high cirrus cloudiness) cases and cirrus-poor (low cirrus cloudiness) cases, respectively. It is noted that the H and L cases in each pair belong to different CWV categories despite that they actually have a similar CWV range. This is because the H-case composite finds itself near the higher end of each specified CWV range while the L composite from the same CWV category ends up near its lower end, owing to the fact that cirrus clouds generally prefer as moist an environment as possible. CWVs lower than 45 mm are not examined because considerable statistical noise due to the rare occurrence of cirrus

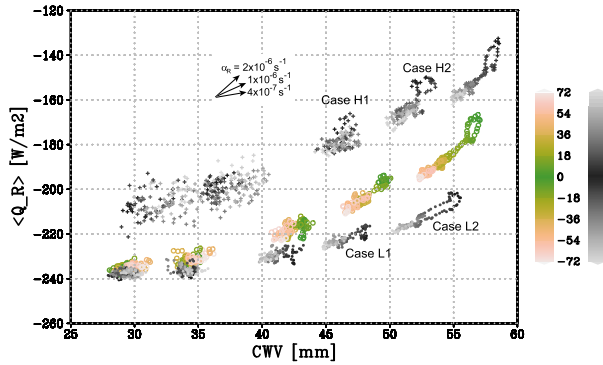


FIG. 5. As in Fig. 3, but with the cirrus-rich and cirrus-poor cases, designated by crosses and filled circles, respectively, both in gray scale. The cases labeled as H1, H2, L1, and L2 are selected for Fig. 6. The control analysis (color), identical to the all-sky cases in Fig. 3, is shown again for comparison (the clear-sky plots are omitted). Arrows are for use later in section 4.

clouds in a dry environment conceals the signal, if it exists, for any systematic evolution.

The composite time series of CWV, SST, and precipitation are presented in Fig. 6 for the selected cases. CWV by design stays close between each pair of cases L1–H1 and L2–H2 (top), except that the cirrus-rich case has a slightly but consistently lower CWV than its cirrus-poor counterpart during ± 12 h around time zero. In SST (middle), cases L1 and H2 are virtually identical while cases L2 and H2 are marginally apart by 0.5°C or less. It is nonetheless found that the disagreement in CWV and SST stays small within each pair compared to across the different pairs, rendering confidence in the aforementioned premise that the L1–H1 and L2–H2 pairs each represent a practically identical thermodynamic environment except radiation.

In spite of the similarity in CWV and SST, the composite evolution of precipitation (bottom) follows distinctly separate paths depending on cirrus cloud cover. The cirrus-rich case therefore gives rise to a precipitation roughly 50% heavier than the cirrus-poor case. This precipitation enhancement is significant in that it distinctly exceeds the standard error of precipitation ($2.9 \times 10^{-4} \text{ mm h}^{-1}$) estimated for the same composite analysis as done in the present analysis (Masunaga 2013). The precipitation peak is slightly earlier than $t = 0$ likely because, as discussed by Masunaga and L'Ecuyer (2014), the time zero is statistically dominated by horizontally extensive events while intensive rainfall is often brought by spatially confined deep convection that typically precedes stratiform anvils. It is difficult to attribute this precipitation excess to a direct moisture effect, recalling that CWV is alike or even smaller for the cirrus-rich cases during the hours of intensified rainfall (Fig. 6, top panel). Rather, the reduction of CWV is more likely a consequence of the

drying effect of the elevated rainfall, while the increase in rainfall is attributed to something other than moisture.

d. The shortwave effects

The radiative heating profiles shown so far are confined to LW cooling by using only the midnight section of *CloudSat*–*CALIPSO* orbits. The results from the afternoon (1330 LT) orbits are outlined here to illustrate the net radiative heating of the atmosphere with the SW effects included in addition to the LW.

Column radiative heating as a function of CWV for the afternoon orbits is plotted in Fig. 7. Additional analysis runs with cirrus-rich and cirrus-poor cases are performed in the same manner as done above for the midnight orbits. It is evident that the inclusion of the SW contribution does not qualitatively alter any fundamental characteristics seen earlier (Fig. 5). Major updates are found in quantitative aspects. SW heating, increasing with CWV, partially offsets or more than cancels LW cooling. The breakdown of the SW effects (not shown) indicates that the water vapor absorption accounts for an increase by $\sim 40 \text{ W m}^{-2}$ while the cloud absorption explains an increase of about 20 W m^{-2} for the entire CWV range studied. It is noted that, since the afternoon overpasses are sampled at an hour of near-peak insolation, the relative strength of the SW effects to their LW counterpart is exaggerated in comparison with the daily mean.

Cirrus-rich (H1 and H2) and cirrus-poor (L1 and L2) composites are constructed from the afternoon samples on the basis of Fig. 7 in the same manner as done for the midnight samples. The evolution of CWV, SST, and precipitation for H1–L1 and H2–L2 cases is shown in Fig. 8 to compare with Fig. 6 above. All major features are surprisingly common to the midnight and afternoon hours, that is, precipitation is systematically heavier when cirrus cloud cover is substantially larger and so is $\langle Q_R \rangle$, despite that CWV and SST are virtually identical or even indicative of less rainfall.

In the following section, we will discuss a possible physical mechanism that explains the Q_R control on tropical rainfall using a simplistic conceptual model.

4. A conceptual model

a. Steady-state energy balance

A fundamental role of radiation in tropical convective dynamics may be glimpsed in the framework originated by Neelin and Held (1987) crudely summarized (with modifications) as follows. The MSE budget in a steady single-column atmosphere is expressed as

$$\langle \omega \partial_p h \rangle = F_T + \langle Q_R \rangle, \quad (1)$$

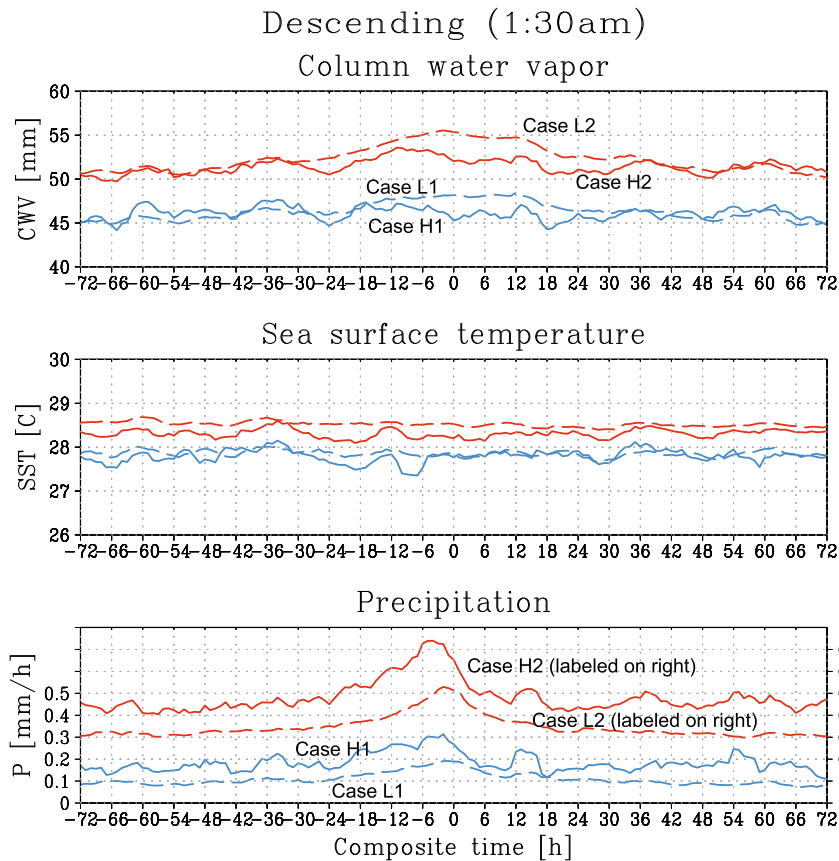


FIG. 6. The composite time series of (top) CWV (mm), (middle) SST ($^{\circ}\text{C}$), and (bottom) surface precipitation (mm h^{-1}) for cases L1 (blue dashed), H1 (blue solid), L2 (red dashed), and H2 (red solid) (see Fig. 5 for the notation). Precipitation for cases L2 and H2 is vertically offset by $+0.2 \text{ mm h}^{-1}$ as labeled on the right axis for visual clarity. Only the descending section of *CloudSat-CALIPSO* orbits is included.

where $\langle \cdot \rangle$ denotes the vertical integral over the whole atmospheric column, h is MSE, F_T designates the surface turbulent fluxes collectively, and ω is vertical pressure velocity. Given the amplitude of vertical velocity $\hat{\omega}$ separated from the structure function $f_{\omega}(p)$ as $\omega(p) \equiv \hat{\omega} f_{\omega}(p)$, (1) provides a measure of large-scale vertical motion in response to the diabatic forcing ($F_T + \langle Q_R \rangle$),

$$\hat{\omega} = \frac{F_T + \langle Q_R \rangle}{\langle f_{\omega} \partial_p h \rangle}. \quad (2)$$

Precipitation is approximately scaled by $\hat{\omega}$ in the tropical atmosphere, as proved by omitting temperature fluctuations and the sensible heat flux in the dry static energy (DSE) budget,

$$LP \approx \hat{\omega} \langle f_{\omega} \partial_p s \rangle, \quad (3)$$

where P is precipitation, L is the specific latent heat of vaporization, and s is DSE. Equations (2) and (3) are combined into

$$LP \approx (F_T + \langle Q_R \rangle) \frac{\langle f_{\omega} \partial_p s \rangle}{\langle f_{\omega} \partial_p h \rangle}. \quad (4)$$

Equations (2) and (4) claim that the large-scale circulation and precipitation are governed by the diabatic forcing in a manner sensitive to vertical atmospheric profiles and the specific form of f_{ω} . This may provide a crude explanation for the precipitation excess under overcast sky as shown by Figs. 5 and 7.

It should be noted that the demonstrations in Figs. 5 and 7 are rather artificial in that each case is forced to have a larger or smaller cloud cover than usual *at all times*. These composite plots are each an idealized representation of perpetually high or low cirrus cloudiness, consistent conceptually with the steady-state thought

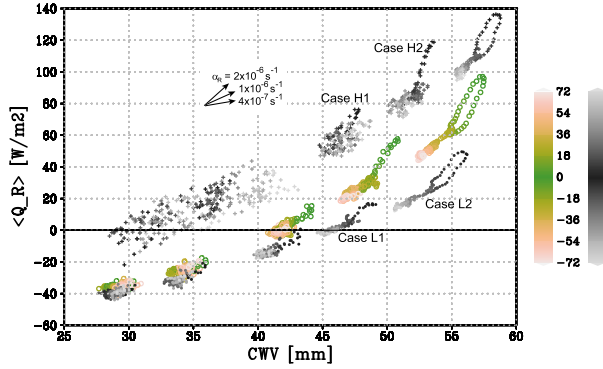


FIG. 7. As in Fig. 5, but for ascending (1330 LT) CloudSat–CALIPSO orbits only.

experiment as above. The real question, however, is whether a gradual increase over time in cirrus cloud cover could impose any radiative impact on the subsequent growth of convection. The observations in this work are not useful for testing this hypothesis, because the composite time series is a collection of originally fragmentary snapshots and thus any information such as anomalous cloudiness at an early hour does not propagate through later hours. Some theoretical thinking is necessary to complement this deficiency.

For this purpose, some premises behind (2) and (3) need to be refined. It has been implicitly assumed that a given, fixed form of f_ω applies universally. In reality, f_ω is by no means invariant but should be given flexibility to account for the transition from shallow updraft to deep ascent. This can be conveniently dealt with by expanding the vertical structure into a series of orthogonal modes, among which the first two baroclinic modes are known to suffice to capture the essential characteristics of tropical convective dynamics (e.g., Mapes and Houze 1995). The second baroclinic mode with lower-tropospheric ascent, or the “congestus mode” (Khouider and Majda 2006), is of particular interest here as a main driver of the dynamics prior to the deep convective burst (Masunaga and L’Ecuyer 2014). The vertical MSE advection associated with the second mode is positive, that is, the second mode imports MSE into the air column, and is therefore no longer able to consume the energy input by the diabatic forcing in a steady balance, necessitating the time-dependent formulation. These requisites are incorporated in a conceptual model discussed next, which is based loosely on the simple model devised by Masunaga and Sumi (2017).

b. Cirrus as a radiative trigger of convection

Masunaga and Sumi (2017) proposed a moisture storage closure characterized by a pair of non-dimensional parameters η_1 and η_2 defined as

$$\begin{aligned} \frac{D\langle q \rangle}{Dt} &= -\eta_1 \langle \omega \partial_p q \rangle_1 - \eta_2 \langle \omega \partial_p q \rangle_2 \\ &\approx -\eta_1 \langle \omega_1 \partial_p q_{bg} \rangle - \eta_2 \langle \omega_2 \partial_p q_{bg} \rangle, \end{aligned} \quad (5)$$

where q is the vapor mixing ratio and $D/Dt \equiv \partial/\partial t + \mathbf{V} \cdot \nabla$ is the Lagrangian derivative operator with respect to horizontal motion. The subscripts 1, 2, and “bg” denote the first and second baroclinic modes and the time-independent background field, respectively. The second equality above holds when the vertical structure of q remains practically preserved during the evolution, leaving the vertical motion solely responsible for the variability of vertical MSE advection. This is in general a justifiable assumption because the vapor mixing ratio anomaly is small in amplitude (less than $1\text{--}2 \text{ g kg}^{-1}$) against the background (cf., Fig. 3 of Masunaga 2013), perhaps with the exception of extreme dry air intrusions. The parameters η_1 and η_2 are the portion of the moisture accumulated by vertical advection that is left behind in the air, and hence loosely measure the inefficiency of rainfall production.

The η parameters have multiple physical interpretations. The reevaporation of condensates is one of the governing factors for η , and the portion of moisture convergence that is not directly fed into cumulus convection is another. As such, η_1 and η_2 summarize a range of the cumulus effects unresolved on a large scale just as conventional cumulus parameterizations do. Chikira (2014) proposed the moistening efficiency (or α in his notation), defined by the ratio of the vertical gradient of moisture to that of DSE, as a convenient tool for diagnosing the moist processes. The α parameter may seem similar in concept to η_1 and η_2 , but the difference lies in that α is a practical measure constructed with reference solely to large-scale sounding rather than serves as a closure assumption.

The congestus mode dominates early stages of the evolution before the first mode sets in (Mapes et al. 2006), so in practice η_2 is of prime importance for studying the effects of cirrus clouds preceding the peak convection. Masunaga and Sumi (2017) found that η_2 is initially close to unity and then decreases as precipitation picks up, that is, the moisture accumulation owing to the second mode is barely convertible into precipitation in the beginning, although this inefficiency is somewhat alleviated later in the evolution.

The basic equation for the present model is the time-dependent, column-integrated MSE budget equation,

$$\frac{D\langle h \rangle}{Dt} = -\langle \omega \partial_p h \rangle + F_T + \langle Q_R \rangle. \quad (6)$$

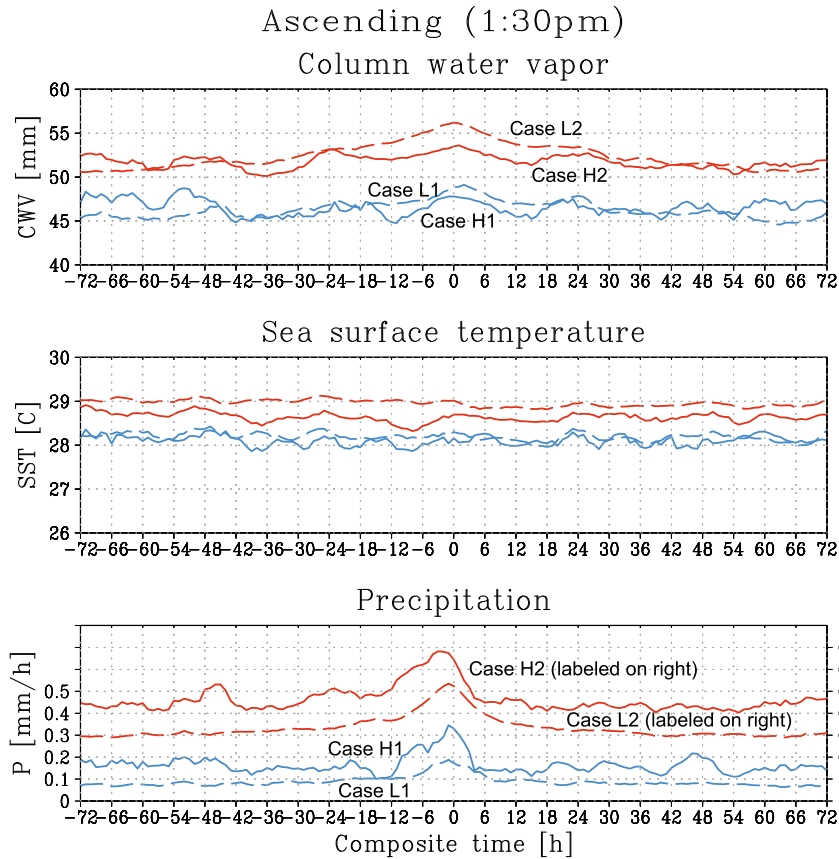


FIG. 8. As in Fig. 6, but for ascending (1330 LT) *CloudSat*-*CALIPSO* orbits only.

By separating the background field out in each variable as $h = h_{\text{bg}} + h'$, where the prime designates the anomaly, (6) is updated as

$$\frac{D\langle h' \rangle}{Dt} = -\langle \omega' \partial_p h_{\text{bg}} \rangle + F'_T + \langle Q'_R \rangle, \quad (7)$$

where the vertical MSE advection is again assumed to arise only from ω' . The background terms are required to satisfy the steady-state MSE balance, (1), on their own and have been subtracted to yield (7). Since ω' is composed of the two baroclinic modes (ω_1 and ω_2) in the current formulation, (7) may be further modified into

$$L \frac{D\langle q' \rangle}{Dt} = \gamma_1 L \langle \omega_1 \partial_p q_{\text{bg}} \rangle + \gamma_2 L \langle \omega_2 \partial_p q_{\text{bg}} \rangle + F'_T + \langle Q'_R \rangle, \quad (8)$$

where the temperature contribution to the MSE tendency has been omitted and

$$\gamma_i \equiv -\frac{\langle \omega_i \partial_p h_{\text{bg}} \rangle}{L \langle \omega_i \partial_p q_{\text{bg}} \rangle} \quad (9)$$

is a version of the normalized gross moist stability (GMS; Raymond et al. 2007) that is here defined individually for the first ($i = 1$) and second ($i = 2$) baroclinic modes. A useful aspect of the mode-specific GMS is that γ_i is time invariant, because the amplitude of ω_i is precisely canceled out in (9). The variability in the surface turbulent flux is outside the present scope in order to focus on the roles of radiative cooling, so hereinafter $F'_T = 0$.

Combining (8) with the moisture storage closure [(5)] in the absence of the first mode (i.e., $\omega_1 = 0$), one finds

$$\left(1 + \frac{\gamma_2}{\eta_2}\right) L \frac{D\langle q' \rangle}{Dt} = \langle Q'_R \rangle. \quad (10)$$

Recalling the systematic dependence of $\langle Q'_R \rangle$ on CWV (Fig. 3), the radiative cooling anomaly is now parameterized explicitly with the CWV anomaly as

$$\langle Q'_R \rangle = \alpha_R L \langle q' \rangle, \quad (11)$$

where α_R is a prescribed coupling constant (s^{-1}). Equations (10) and (11) together lead to a concise prognostic equation to predict the CWV anomaly as

$$\frac{D\langle q' \rangle}{Dt} = \frac{\alpha_R}{1 + \frac{\gamma_2}{\eta_2}} \langle q' \rangle. \quad (12)$$

For comparison, another equation of the same form is derived for the first mode by assuming $\omega_2 = 0$ as

$$\frac{D\langle q' \rangle}{Dt} = \frac{\alpha_R}{1 + \frac{\gamma_1}{\eta_1}} \langle q' \rangle. \quad (13)$$

Equations (12) and (13) may be interpreted to be an asymptotic realization of the moisture evolution before the deep convective onset (i.e., $\omega_1 = 0$) and during the peak convective activity ($\omega_2 = 0$), respectively. The formal solution of the CWV anomaly for a Lagrangian air column is readily found to be

$$\langle q' \rangle = \langle q' \rangle_0 \exp(\tau_R t), \quad \text{where } \tau_R \equiv \frac{1}{\alpha_R} \left(1 + \frac{\gamma}{\eta} \right), \quad (14)$$

where $\langle q' \rangle_0$ is the initial condition of $\langle q' \rangle$. The subscript of γ and η is now omitted so (14) represents the generalized solution for the two idealized setups individually.

The solution (14) claims that the CWV anomaly grows or decays with time at the e -folding rate of τ_R . Figure 9 shows the growth rate of $\langle q' \rangle$ (or the inverse of τ_R) as a function of η for $\alpha_R = 4 \times 10^{-7}, 1 \times 10^{-6},$ and $2 \times 10^{-6} \text{ s}^{-1}$. These three numbers, indicated by arrows in Fig. 5, are chosen to cover a realistic range of the observed sensitivity of $\langle Q_R \rangle$ to CWV. For each α_R , $\tau_R^{-1}(\eta)$ is depicted for $\gamma_2 = -0.5$ and $\gamma_1 = 0.2$ correspondingly to (12) and (13). These values of γ_1 and γ_2 were determined from in situ soundings over the tropical Indian Ocean (Masunaga and Sumi 2017). The above choice of γ_1 and γ_2 may be considered to be representative of tropical atmospheres in general.

The most outstanding feature in Fig. 9 is that the growth rate for the second mode has a sharp rise as η approaches 0.5 from above, as expected from (14), where τ_R^{-1} is diverged to infinity for $\eta \rightarrow -\gamma$. This behavior has a close relevance to the instability induced by negative GMS as discussed extensively by Raymond et al. (2009). Such an instability occurs when $\gamma + \eta$ diminishes to below zero in the current formulation, with the growth rate beginning to climb dramatically as η decreases to the vicinity of $-\gamma$ or 0.5. Figure 9 shows that τ_R for the second mode reaches about 50 h at $\eta \approx 0.8$ for $\alpha_R = 2 \times 10^{-6} \text{ s}^{-1}$ and 100 h or longer for the smaller values of α_R . Given that η_2 does not descend far below 0.8 in reality (Masunaga and Sumi 2017), these values set the upper limit to the realistic growth rate in practice for each setup of α_R .

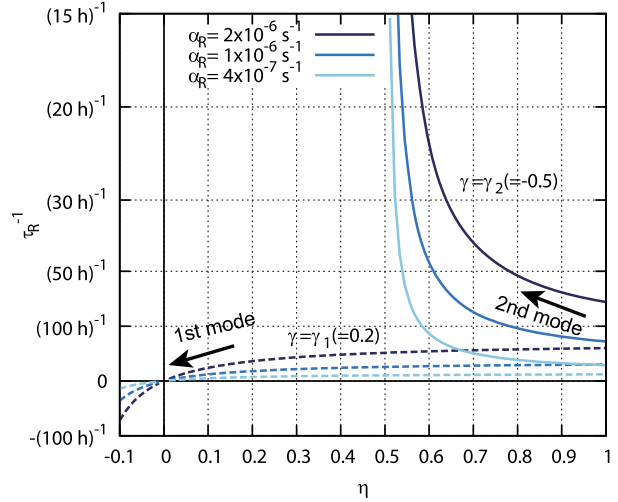


FIG. 9. The growth rate of CWV anomaly τ_R^{-1} plotted against the moisture storage ratio η . Solid and dashed curves show the second baroclinic mode ($\gamma = -0.5$) and the first mode ($\gamma = 0.2$), respectively, for $\alpha_R = 4 \times 10^{-7}, 1 \times 10^{-6},$ and $2 \times 10^{-6} \text{ s}^{-1}$ as designated in the key. Arrows indicate the direction of the temporal evolution prior to the peak convection (see text for details).

The growth rate is in theory allowed to rise limitlessly if η decreases to 0.5, but this is unlikely to occur in the real atmosphere. The assumption of $\omega_1 = 0$ is ruled out as the evolution proceeds further and the second mode gives way to the first mode. Once the first mode exceeds the second in magnitude, the growth rate follows that of the first mode (dashed lines in Fig. 9), implying only a very slow growth of CWV anomaly ($\tau_R \gg 100 \text{ h}$) regardless of η and α_R .

The contrasting behaviors between the first and second modes may be understood as follows. A moist anomaly introduced by vertical moisture advection is translated into an increase of $\langle Q_R \rangle$ through (11), which in turn feeds back on the initial perturbation according to the MSE conservation law [(8)]. When the second mode dominates, the air column imports MSE and moisture at the same time (i.e., γ being negative) and hence is capable to dynamically amplify the low-level ascent fed by the radiative heating anomaly. On the contrary, vertical MSE advection is negative and thus offsets, rather than amplifies, the $\langle Q_R \rangle$ forcing for a deep ascent associated with the first mode. The competition between the export of MSE and column radiative heating is central of the theory developed by Raymond and Zeng (2000), who indeed found a growth over a time scale of a few 100 h. This time scale is far too long in light of the life time of convective systems, and is instead relevant to the weekly to intraseasonal variabilities. Recall that the growth time is as short as 2 days when the dynamics is driven by the congestus mode, offering a

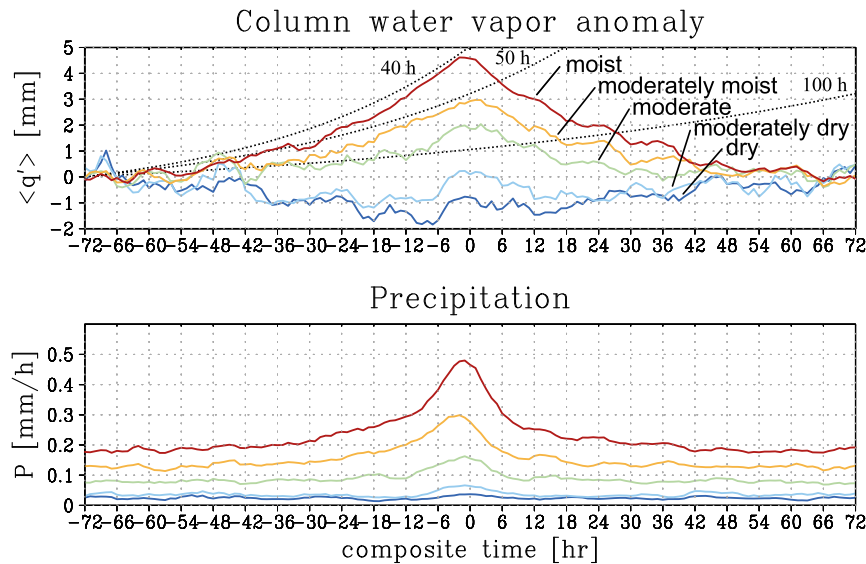


FIG. 10. (top) The composite time series of the CWV anomaly for the five moisture classes as indicated. The anomaly is calculated with respect to the background level defined as the temporal mean of the first and last 12 h combined. Three dashed lines show theoretical curves with $\tau_R = 40, 50,$ and 100 h, from top to bottom, as a reference. (bottom) The composite time series of precipitation.

potential mechanism triggering the growth of individual convective systems through the swift accumulation of moisture.

It is expected that the growth time depends on the ambient moisture, recalling that α_R monotonically increases with CWV (Fig. 5). To confirm this, the observed time series of the CWV anomaly is plotted in Fig. 10. The anomaly is computed against the background level defined as the temporal mean of the first and last 12 h combined together for each moisture class. The CWV anomaly increases over time toward time zero at a rate varying with the ambient moisture. The theoretical prediction given by (14) is also depicted as a reference for $\tau_R = 40, 50,$ and 100 h, where the equation is slightly modified to $\exp[(t + 72\text{ h})/\tau_R] - 1$ so it matches the present format. A very humid atmosphere experiences a notable moistening prior to the peak convection, consistent with an elevated growth rate as predicted ($\tau_R \sim 40\text{--}50$ h) when α_R is large. On the other hand, the CWV anomaly stays neutral or even slightly decreases during the same hours in dry atmospheres (the dry and moderately dry curves in Fig. 10). The muted moistening in a dry environment is explained by the dependence of τ_R on α_R as depicted by Fig. 9.

The slight drying might be ascribed to the negative CRE as seen in Fig. 3. A negative CRE implies a negative α_R if cloudiness is positively correlated with CWV, in which case a moist anomaly would decay with time according to (14). Although not explicitly included in

the present model, the shallow-cumulus mode, representing shallow updraft just above the boundary layer, is arguably the dominant vertical mode in dry atmospheres and may act to maintain the dry state in a stable manner (Masunaga 2014).

The simple theory and the analysis results above confirm the possibility that the congestus mode could give rise to a significant moistening when coupled with a radiative heating anomaly brought by cirrus clouds. This could be a trigger of the subsequent pickup of precipitation. In Fig. 10 (bottom panel), the sharp rise of precipitation is striking in a humid environment while minimal when the ambient air is dry, echoing the CWV dependence of cloud cover profiles presented in Fig. 1. It confirms that radiation can be a key factor for intensifying convection and that the cirrus clouds leading the onset of convection are a major source of the radiative perturbation.

5. Summary and discussion

Satellite observations are exploited in search of possible evidence for radiative–convective interactions with focus on the hourly to daily variability intrinsic to the life time of convective systems over tropical oceans. To this end, *CloudSat–CALIPSO* snapshots of the vertical cloud structure are projected onto a composite time series centered around the moments of convective occurrence identified by the TRMM PR. Such a composite

technique has been demonstrated to be useful for illustrating the systematic change of large-scale atmospheric state associated with the development and dissipation of convective systems (e.g., Masunaga 2012). The composite time series are broken down by CWV at time zero in order to test different radiative environments individually. It is confirmed that clouds are bound below ~ 2 km when the ambient air is very dry while vertical developing convection is present in a moist atmosphere. Cirrus clouds are prevailing in the moist environment, accompanied by a modest enhancement in cloud cover before and after the peak convection with a slight temporal asymmetry in which the leading cirrus slightly exceeds the trailing cirrus.

The preceding cirrus clouds could in theory have multiple origins. Cirrus clouds detrained from an existing convective system nearby may be transported into the target area before the parent system eventually marches in, as reported by past observational work (e.g., Yamada et al. 2010). The present composite technique by design applies to the Eulerian frame, and it is difficult to assess to what extent the intruding cirrus may be aliased into the time series. Another possible origin is the in situ formation of cirrus clouds, which accounts for more than a half of tropical cirrus clouds (Luo and Rossow 2004). Johnson et al. (2015) found evidence for cirrus formation in response to the Kelvin-wave induced cool anomalies prior to the MJO convective burst and discussed its radiative impact on the local energy budget. Their analysis may suggest the prior development of cirrus may influence the convection on a broad range of time scales. The third potential source of the preceding cirrus is the detrainment from scattered deep convection prevailing over tropical oceans. Isolated cumuli themselves may be barely discernible in cloud cover shown by Fig. 1, but the cirrus clouds they produce could begin to fill in a large-scale domain at some point in the evolution. While it is unable to single out where the leading cirrus comes from, this study finds that cirrus clouds have physical consequences on the subsequent evolution of convection irrespective of their origins.

Composite analysis runs with descending (0130 LT) A-Train orbits show that LW cooling is heavily suppressed by developing clouds in a humid environment, while very efficient owing to the absence of cirrus clouds when the ambient air is dry. The CRE is even negative in a very dry environment, where the LW emissions from low clouds are hardly absorbed as they escape to space and thus an increase in low cloud cover would enhance the LW cooling. The composite trajectories appear to be lined up practically on a unique, continuous curve across a broad range of CWV when projected onto the $\langle Q_R \rangle$ -CWV plane. This may imply a universal

relationship between CRE and CWV and hence that the cloud optical properties and cloud-top-height distribution may be somehow tightly coupled with CWV.

The composite statistics, however, exhibit significant spread: the “universal” curve is split when the composite samples are divided into those with a high cirrus cloudiness and the others with a low cirrus cloudiness on the basis of the cloudiness at 13 km in each hour along the time axis. Two pairs of these cirrus-rich and cirrus-poor composites each under a similar CWV range are selected as a test bed for isolating the radiative effects from the direct moisture effects on convection. Precipitation is found to be distinctly heavier when cirrus cloud cover is larger despite that the moisture environment is virtually identical, suggestive of a link between the radiative perturbation by cirrus clouds and the convective intensity. Another set of analysis runs with ascending A-Train orbits (i.e., the SW effects included) arrives at the same conclusion in a qualitative sense.

The physical basis behind this radiative–convective linkage may be understood to the zeroth-order approximation in terms of the MSE budget. If the variability in the surface turbulent flux is small, a fluctuation in column radiative heating should be balanced against the MSE export associated with large-scale ascent (and therefore precipitation). The sensible and latent heat fluxes abruptly increase by 15–20 and 30–70 W m^{-2} , respectively, around the peak convection (Yokoi et al. 2014), which could momentarily reinforce the effect of $\langle Q_R \rangle$ on the MSE budget during a limited period of time (a few hours) with enhanced gustiness. The large-scale motion is often considered in the relevant literature (Neelin and Held 1987; Raymond and Zeng 2000) to be a deep ascent represented by the first baroclinic mode. The present simple model describing the evolution of the CWV anomaly yields a growth time much longer than 100 h when the large-scale motion is governed by the first baroclinic mode. This does not contradict the fact that a radiative–convective feedback takes a weekly or intraseasonal time scale to occur in existing studies. The present analysis sheds light on the importance of the second baroclinic (or congestus) mode, which gives rise to a rapid coupling of cirrus-induced radiative effects with convective dynamics. This mechanism has the potential to help improve our understanding of the link between cirrus clouds and atmospheric circulation, which remains a key problem in climate simulations (Bony et al. 2015).

Although beyond the current single-column framework, it may be argued that the horizontal radiative gradient between cloudy and cloud-free domains possibly plays an additional role in driving the overturning circulation. Recent studies revealed that a radiatively driven subsidence

owing to longwave emissions by low clouds is a crucial process for the convective self-aggregation to make progress (e.g., Holloway et al. 2017). Such a subsidence induces a shallow circulation across moist and dry regions (Coppin and Bony 2015), which has the potential to strengthen the congestus-mode dynamics discussed in this work.

The radiative–convective interactions are important for MJO not only during the convectively active phase in which the first mode governs the local dynamics, but play a distinct role in weakly precipitating periods (Kim et al. 2015). This is in line with the present finding that the cirrus radiative effects are of particular importance when the congestus (or the second baroclinic) mode is dominant. The congestus mode could amplify the CWV anomaly at a growth time as short as ~ 50 h in moist atmospheres, because shallow circulation having a negative GMS (Back and Bretherton 2006) is prone by nature to grow on its own. The congestus mode is a fast-working agent of radiative–convective interactions, which arguably helps invigorate the convective activity within a period of a few days when assisted radiatively by the preceding cirrus clouds.

Acknowledgments. The authors are grateful to Jean-Yves Grandpeix, Dave Thompson, Dave Randall, Dick Johnson, Johnny Luo, Claudia Stubenrauch, Caroline Muller, Chris Kummerow, and three anonymous reviewers for their comments, which helped enrich aspects of the discussions presented in the paper. This work is supported by Japan Society for the Promotion of Science (JSPS) Grants-in-Aid for Scientific Research (KAKENHI) Fund for the Promotion of Joint International Research Development (15KK0157) and the European Research Council (Grant Agreement 694768). The *CloudSat*–*CALIPSO* data products were provided by the *CloudSat* Data Processing Center (<http://www.CloudSat.cira.colostate.edu>),

the TRMM PR dataset by the Japan Aerospace Exploration Agency (JAXA; <https://www.gportal.jaxa.jp/gp/top.html>), and the TRMM TMI and AMSR-E products by Remote Sensing Systems (<http://www.remss.com>).

APPENDIX

Temporal Asymmetry of Cirrus Cloud Cover

The central interest of this work is the cirrus increase 1–2 days prior to deep convection, especially in the context of its potential radiative impacts on the subsequent development of convection. One might argue that the leading cirrus could be a statistical artifact due to sampling noise, with the possibility in mind that the TRMM may detect precipitation at later stages of the convective life cycle when anvil clouds have already grown extensively. With the assumption that such stochastic spread over time is random by nature, the signals of preceding cirrus are tested for robustness by decomposing cloud cover f_c into the temporally symmetric and asymmetric components, f_{sym} and f_{asym} , respectively, as

$$f_{\text{sym}}(t) = \frac{f_c(t_0 + t) + f_c(t_0 - t)}{2} \quad \text{and}$$

$$f_{\text{asym}}(t) = \frac{f_c(t_0 + t) - f_c(t_0 - t)}{2} \quad \text{for } t \geq 0,$$

where t_0 refers to the hour of the peak precipitation (roughly around 0 h). Figure A1 shows each of the two components for the moist case obtained from the bottom panel of Fig. 1. While a positive asymmetry (i.e., more cloudiness after the peak than before) above 4 km implies stratiform precipitation dominating the mature phase of the convective life cycle, a negative asymmetry takes over for $t > 12$ h above 12 km, suggesting that the preceding cirrus should embody a real entity beyond a sampling artifact.

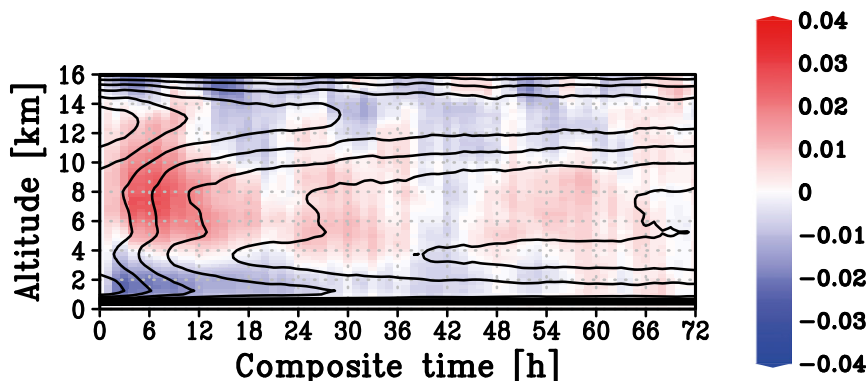


FIG. A1. The temporally symmetric (contour) and asymmetric (color shaded) components of *CloudSat*–*CALIPSO* cloud cover about the time of peak precipitation (see text for definitions) for the moist case. The contour interval is 0.05.

REFERENCES

- Back, L. E., and C. S. Bretherton, 2006: Geographic variability in the export of moist static energy and vertical motion profiles in the tropical Pacific. *Geophys. Res. Lett.*, **33**, L17810, <https://doi.org/10.1029/2006GL026672>.
- Bony, S., and K. A. Emanuel, 2005: On the role of moist processes in tropical intraseasonal variability: Cloud–radiation and moisture–convection feedbacks. *J. Atmos. Sci.*, **62**, 2770–2789, <https://doi.org/10.1175/JAS3506.1>.
- , and Coauthors, 2015: Clouds, circulation and climate sensitivity. *Nat. Geosci.*, **8**, 261–268, <https://doi.org/10.1038/ngeo2398>.
- , B. Stevens, D. Coppin, T. Becker, K. A. Reed, A. Voigt, and B. Medeiros, 2016: Thermodynamic control of anvil cloud amount. *Proc. Natl. Acad. Sci. USA*, **113**, 8927–8932, <https://doi.org/10.1073/pnas.1601472113>.
- Bretherton, C. S., P. N. Blossey, and M. Khairoutdinov, 2005: An energy-balance analysis of deep convective self-aggregation above uniform SST. *J. Atmos. Sci.*, **62**, 4273–4292, <https://doi.org/10.1175/JAS3614.1>.
- Brown, R. G., and C. D. Zhang, 1997: Variability of midtropospheric moisture and its effect on cloud-top height distribution during TOGA COARE. *J. Atmos. Sci.*, **54**, 2760–2774, [https://doi.org/10.1175/1520-0469\(1997\)054<2760:VOMMAI>2.0.CO;2](https://doi.org/10.1175/1520-0469(1997)054<2760:VOMMAI>2.0.CO;2).
- Chen, S. S., and R. A. Houze Jr., 1997: Diurnal variation and life-cycle of deep convective systems over the tropical Pacific warm pool. *Quart. J. Roy. Meteor. Soc.*, **123**, 357–388, <https://doi.org/10.1002/qj.49712353806>.
- Chikira, M., 2014: Eastward-propagating intraseasonal oscillation represented by Chikira–Sugiyama cumulus parameterization. Part II: Understanding moisture variation under weak temperature gradient balance. *J. Atmos. Sci.*, **71**, 615–639, <https://doi.org/10.1175/JAS-D-13-038.1>.
- Ciesielski, P. E., R. H. Johnson, P. T. Haertel, and J. Wang, 2003: Corrected TOGA COARE sounding humidity data: Impact on diagnosed properties of convection and climate over the warm pool. *J. Climate*, **16**, 2370–2384, <https://doi.org/10.1175/2790.1>.
- Coppin, D., and S. Bony, 2015: Physical mechanisms controlling the initiation of convective self-aggregation in a general circulation model. *J. Adv. Model. Earth Syst.*, **7**, 2060–2078, <https://doi.org/10.1002/2015MS000571>.
- Fermepin, S., and S. Bony, 2014: Influence of low-cloud radiative effects on tropical circulation and precipitation. *J. Adv. Model. Earth Syst.*, **6**, 513–526, <https://doi.org/10.1002/2013MS000288>.
- Gray, W. M., and R. W. Jacobson Jr., 1977: Diurnal variation of deep cumulus convection. *Mon. Wea. Rev.*, **105**, 1171–1188, [https://doi.org/10.1175/1520-0493\(1977\)105<1171:DVOGCC>2.0.CO;2](https://doi.org/10.1175/1520-0493(1977)105<1171:DVOGCC>2.0.CO;2).
- Haladay, T., and G. Stephens, 2009: Characteristics of tropical thin cirrus clouds deduced from joint *CloudSat* and *CALIPSO* observations. *J. Geophys. Res.*, **114**, D00A25, <https://doi.org/10.1029/2008JD010675>.
- Hartmann, D. L., and K. Larson, 2002: An important constraint on tropical cloud - climate feedback. *Geophys. Res. Lett.*, **29**, 1951, <https://doi.org/10.1029/2002GL015835>.
- Henderson, D. S., T. S. L'Ecuyer, G. Stephens, P. Partain, and M. Sekiguchi, 2013: A multisensor perspective on the radiative impacts of clouds and aerosols. *J. Appl. Meteor. Climatol.*, **52**, 853–871, <https://doi.org/10.1175/JAMC-D-12-025.1>.
- Holloway, C. E., A. A. Wing, S. Bony, C. Muller, H. Masunaga, T. S. L'Ecuyer, D. D. Turner, and P. Zuidema, 2017: Observing convective aggregation. *Surv. Geophys.*, **38**, 1199–1236, <https://doi.org/10.1007/s10712-017-9419-1>.
- Houze, R. A., Jr., 1982: Cloud clusters and large-scale vertical motions in the tropics. *J. Meteor. Soc. Japan*, **60**, 396–410, https://doi.org/10.2151/jmsj1965.60.1_396.
- , 2004: Mesoscale convective systems. *Rev. Geophys.*, **42**, RG4003, <https://doi.org/10.1029/2004RG000150>.
- Hu, Q., and D. A. Randall, 1994: Low-frequency oscillations in radiative-convective systems. *J. Atmos. Sci.*, **51**, 1089–1099, [https://doi.org/10.1175/1520-0469\(1994\)051<1089:LFOIRC>2.0.CO;2](https://doi.org/10.1175/1520-0469(1994)051<1089:LFOIRC>2.0.CO;2).
- Jensen, M. P., and A. D. Del Genio, 2006: Factors limiting convective cloud-top height at the ARM Nauru Island climate research facility. *J. Climate*, **19**, 2105–2117, <https://doi.org/10.1175/JCLI3722.1>.
- Johnson, R. H., P. E. Ciesielski, J. H. Ruppert Jr., and M. Katsumata, 2015: Sounding-based thermodynamic budgets for DYNAMO. *J. Atmos. Sci.*, **72**, 598–622, <https://doi.org/10.1175/JAS-D-14-0202.1>.
- Khouider, B., and A. J. Majda, 2006: A simple multicloud parameterization for convectively coupled tropical waves. Part I: Linear analysis. *J. Atmos. Sci.*, **63**, 1308–1323, <https://doi.org/10.1175/JAS3677.1>.
- Kim, D., M. Ahn, I. Kang, and A. D. Del Genio, 2015: Role of longwave cloud–radiation feedback in the simulation of the Madden–Julian oscillation. *J. Climate*, **28**, 6979–6994, <https://doi.org/10.1175/JCLI-D-14-00767.1>.
- Kummerow, C. D., W. Barnes, T. Kozu, J. Shiue, and J. Simpson, 1998: The Tropical Rainfall Measuring Mission (TRMM) sensor package. *J. Atmos. Oceanic Technol.*, **15**, 809–817, [https://doi.org/10.1175/1520-0426\(1998\)015<0809:TTRMMT>2.0.CO;2](https://doi.org/10.1175/1520-0426(1998)015<0809:TTRMMT>2.0.CO;2).
- L'Ecuyer, T. S., N. B. Wood, T. Haladay, G. L. Stephens, and P. W. Stackhouse Jr., 2008: Impact of clouds on atmospheric heating based on the R04 *CloudSat* fluxes and heating rates data set. *J. Geophys. Res.*, **113**, D00A15, <https://doi.org/10.1029/2008JD009951>.
- , and Coauthors, 2015: The observed state of the energy budget in the early twenty-first century. *J. Climate*, **28**, 8319–8346, <https://doi.org/10.1175/JCLI-D-14-00556.1>.
- Lee, M.-I., I.-S. Kang, J.-K. Kim, and B. E. Mapes, 2001: Influence of cloud-radiation interaction on simulating tropical intraseasonal oscillation with an atmospheric general circulation model. *J. Geophys. Res.*, **106**, 14 219–14 233, <https://doi.org/10.1029/2001JD900143>.
- Li, W., C. Schumacher, and S. A. McFarlane, 2013: Radiative heating of the ISCCP upper level cloud regimes and its impact on the large-scale tropical circulation. *J. Geophys. Res. Atmos.*, **118**, 592–604, <https://doi.org/10.1002/jgrd.50114>.
- Lin, J., B. Mapes, M. Zhang, and M. Newman, 2004: Stratiform precipitation, vertical heating profiles, and the Madden–Julian oscillation. *J. Atmos. Sci.*, **61**, 296–309, [https://doi.org/10.1175/1520-0469\(2004\)061<0296:SPVHPA>2.0.CO;2](https://doi.org/10.1175/1520-0469(2004)061<0296:SPVHPA>2.0.CO;2).
- Lindzen, R. S., M.-D. Chou, and A. Y. Hou, 2001: Does the Earth have an adaptive infrared iris? *Bull. Amer. Meteor. Soc.*, **82**, 417–432, [https://doi.org/10.1175/1520-0477\(2001\)082<0417:DTEHAA>2.3.CO;2](https://doi.org/10.1175/1520-0477(2001)082<0417:DTEHAA>2.3.CO;2).
- Luo, Z., and W. B. Rossow, 2004: Characterizing tropical cirrus life cycle, evolution, and interaction with upper-tropospheric water vapor using Lagrangian trajectory analysis of satellite observations. *J. Climate*, **17**, 4541–4563, <https://doi.org/10.1175/3222.1>.
- Mace, G. G., Q. Zhang, M. Vaughan, R. Marchand, G. Stephens, C. Trepte, and D. Winker, 2009: A description of hydrometeor layer occurrence statistics derived from the first year of merged *CloudSat* and *CALIPSO* data. *J. Geophys. Res.*, **114**, D00A26, <https://doi.org/10.1029/2007JD009755>.

- Mapes, B. E., and R. A. Houze Jr., 1995: Diabatic divergence profiles in western Pacific mesoscale convective systems. *J. Atmos. Sci.*, **52**, 1807–1828, [https://doi.org/10.1175/1520-0469\(1995\)052<1807:DDPIWP>2.0.CO;2](https://doi.org/10.1175/1520-0469(1995)052<1807:DDPIWP>2.0.CO;2).
- , S. Tulich, J. Lin, and P. Zuidema, 2006: The mesoscale convection life cycle: Building block or prototype for large-scale tropical waves? *Dyn. Atmos. Oceans*, **42**, 3–29, <https://doi.org/10.1016/j.dynatmoce.2006.03.003>.
- Masunaga, H., 2012: A satellite study of the atmospheric forcing and response to moist convection over tropical and subtropical oceans. *J. Atmos. Sci.*, **69**, 150–167, <https://doi.org/10.1175/JAS-D-11-016.1>.
- , 2013: A satellite study of tropical moist convection and environmental variability: A moisture and thermal budget analysis. *J. Atmos. Sci.*, **70**, 2443–2466, <https://doi.org/10.1175/JAS-D-12-0273.1>.
- , 2014: Free-tropospheric moisture convergence and tropical convective regimes. *Geophys. Res. Lett.*, **41**, 8611–8618, <https://doi.org/10.1002/2014GL062301>.
- , and T. S. L'Ecuyer, 2014: A mechanism of tropical convection inferred from observed variability in the moist static energy budget. *J. Atmos. Sci.*, **71**, 3747–3766, <https://doi.org/10.1175/JAS-D-14-0015.1>.
- , and Y. Sumi, 2017: A toy model of tropical convection with a moisture storage closure. *J. Adv. Model. Earth Syst.*, **9**, 647–667, <https://doi.org/10.1002/2016MS000855>.
- Muller, C. J., and I. M. Held, 2012: Detailed investigation of the self-aggregation of convection in cloud-resolving simulations. *J. Atmos. Sci.*, **69**, 2551–2565, <https://doi.org/10.1175/JAS-D-11-0257.1>.
- Neelin, J. D., and I. M. Held, 1987: Modeling tropical convergence based on the moist static energy budget. *Mon. Wea. Rev.*, **115**, 3–12, [https://doi.org/10.1175/1520-0493\(1987\)115<0003:MTCBOT>2.0.CO;2](https://doi.org/10.1175/1520-0493(1987)115<0003:MTCBOT>2.0.CO;2).
- Nilsson, J., and K. A. Emanuel, 1999: Equilibrium atmospheres of a two-column radiative-convective model. *Quart. J. Roy. Meteor. Soc.*, **125**, 2239–2264, <https://doi.org/10.1002/qj.49712555814>.
- Numaguti, A., R. Oki, K. Nakamura, K. Tsuboki, N. Misawa, T. Asai, and Y. M. Kodama, 1995: 4–5-day-period variation and low-level dry air observed in the equatorial western Pacific during the TOGA-COARE IOP. *J. Meteor. Soc. Japan*, **73**, 267–290, https://doi.org/10.2151/jmsj1965.73.2B_267.
- Ramanathan, V., and W. Collins, 1991: Thermodynamic regulation of ocean warming by cirrus clouds deduced from observations of the 1987 El Niño. *Nature*, **351**, 27–32, <https://doi.org/10.1038/351027a0>.
- Randall, D. A., Harshvardhan, D. A. Dazlich, and T. G. Corsetti, 1989: Interactions among radiation, convection, and large-scale dynamics in a general circulation model. *J. Atmos. Sci.*, **46**, 1943–1970, [https://doi.org/10.1175/1520-0469\(1989\)046<1943:IARCAL>2.0.CO;2](https://doi.org/10.1175/1520-0469(1989)046<1943:IARCAL>2.0.CO;2).
- Raymond, D. J., 2000: The Hadley circulation as a radiative-convective instability. *J. Atmos. Sci.*, **57**, 1286–1297, [https://doi.org/10.1175/1520-0469\(2000\)057<1286:THCAAR>2.0.CO;2](https://doi.org/10.1175/1520-0469(2000)057<1286:THCAAR>2.0.CO;2).
- , 2001: A new model of the Madden-Julian oscillation. *J. Atmos. Sci.*, **58**, 2807–2819, [https://doi.org/10.1175/1520-0469\(2001\)058<2807:ANMOTM>2.0.CO;2](https://doi.org/10.1175/1520-0469(2001)058<2807:ANMOTM>2.0.CO;2).
- , and X. Zeng, 2000: Instability and large-scale circulations in a two-column model of the tropical troposphere. *Quart. J. Roy. Meteor. Soc.*, **126**, 3117–3135, <https://doi.org/10.1002/qj.49712657007>.
- , S. L. Sessions, and Z. Fuchs, 2007: A theory for the spinup of tropical depressions. *Quart. J. Roy. Meteor. Soc.*, **133**, 1743–1754, <https://doi.org/10.1002/qj.125>.
- , —, A. H. Sobel, and Z. Fuchs, 2009: The mechanics of gross moist stability. *J. Adv. Model. Earth Syst.*, **1** (9), <https://doi.org/10.3894/JAMES.2009.1.9>.
- Sherwood, S. C., 1999: Convective precursors and predictability in the tropical western Pacific. *Mon. Wea. Rev.*, **127**, 2977–2991, [https://doi.org/10.1175/1520-0493\(1999\)127<2977:CPAPIT>2.0.CO;2](https://doi.org/10.1175/1520-0493(1999)127<2977:CPAPIT>2.0.CO;2).
- Sobel, A. H., and H. Gildor, 2003: A simple time-dependent model of SST hot spots. *J. Climate*, **16**, 3978–3992, [https://doi.org/10.1175/1520-0442\(2003\)016<3978:ASTMOS>2.0.CO;2](https://doi.org/10.1175/1520-0442(2003)016<3978:ASTMOS>2.0.CO;2).
- Stephens, G. L., S. van den Heever, and L. Pakula, 2008: Radiative-convective feedbacks in idealized states of radiative-convective equilibrium. *J. Atmos. Sci.*, **65**, 3899–3916, <https://doi.org/10.1175/2008JAS2524.1>.
- Tao, W.-K., S. Lang, J. Simpson, C.-H. Sui, B. Ferrier, and M.-D. Chou, 1996: Mechanisms of cloud-radiation interaction in the tropics and midlatitude. *J. Atmos. Sci.*, **53**, 2624–2651, [https://doi.org/10.1175/1520-0469\(1996\)053<2624:MOCRII>2.0.CO;2](https://doi.org/10.1175/1520-0469(1996)053<2624:MOCRII>2.0.CO;2).
- , D. Johnson, C.-L. Shie, and J. Simpson, 2004: The atmospheric energy budget and large-scale precipitation efficiency of convective systems during TOGA COARE, GATE, SCSMEX, and ARM: Cloud-resolving model simulations. *J. Atmos. Sci.*, **61**, 2405–2423, [https://doi.org/10.1175/1520-0469\(2004\)061<2405:TAEBAL>2.0.CO;2](https://doi.org/10.1175/1520-0469(2004)061<2405:TAEBAL>2.0.CO;2).
- Tompkins, A. M., and G. C. Craig, 1998: Radiative-convective equilibrium in a three-dimensional cloud-ensemble model. *Quart. J. Roy. Meteor. Soc.*, **124**, 2073–2097, <https://doi.org/10.1002/qj.49712455013>.
- Trenberth, K. E., J. T. Fasullo, and J. Kiehl, 2009: Earth's global energy budget. *Bull. Amer. Meteor. Soc.*, **90**, 311–323, <https://doi.org/10.1175/2008BAMS2634.1>.
- Webster, P. J., and G. L. Stephens, 1980: Tropical upper-tropospheric extended clouds: Inferences from winter MONEX. *J. Atmos. Sci.*, **37**, 1521–1541, <https://doi.org/10.1175/1520-0469-37.7.1521>.
- Wetherald, R. T., and S. Manabe, 1988: Cloud feedback processes in a general circulation model. *J. Atmos. Sci.*, **45**, 1397–1415, [https://doi.org/10.1175/1520-0469\(1988\)045<1397:CFPIAG>2.0.CO;2](https://doi.org/10.1175/1520-0469(1988)045<1397:CFPIAG>2.0.CO;2).
- Wing, A. A., and K. A. Emanuel, 2014: Physical mechanisms controlling self-aggregation of convection in idealized numerical modeling simulations. *J. Adv. Model. Earth Syst.*, **6**, 59–74, <https://doi.org/10.1002/2013MS000269>.
- Xu, K.-M., and D. A. Randall, 1995: Impact of interactive radiative transfer on the macroscopic behavior of cumulus ensembles. Part II: Mechanisms for cloud-radiation interactions. *J. Atmos. Sci.*, **52**, 800–817, [https://doi.org/10.1175/1520-0469\(1995\)052<0800:IOIRTO>2.0.CO;2](https://doi.org/10.1175/1520-0469(1995)052<0800:IOIRTO>2.0.CO;2).
- Yamada, H., K. Yoneyama, M. Katsumata, and R. Shirooka, 2010: Observations of a super cloud cluster accompanied by synoptic-scale eastward-propagating precipitating systems over the Indian Ocean. *J. Atmos. Sci.*, **67**, 1456–1473, <https://doi.org/10.1175/2009JAS3151.1>.
- Yasunaga, K., and Coauthors, 2006: Melting layer cloud observed during R/V *Mirai* cruise MR01-K05. *J. Atmos. Sci.*, **63**, 3020–3032, <https://doi.org/10.1175/JAS3779.1>.
- Yokoi, S., M. Katsumata, and K. Yoneyama, 2014: Variability in surface meteorology and air-sea fluxes due to cumulus convective systems observed during CINDY/DYNAMO. *J. Geophys. Res. Atmos.*, **119**, 2064–2078, <https://doi.org/10.1002/2013JD020621>.
- Yoneyama, K., and T. Fujitani, 1995: The behavior of dry westerly air associated with convection observed during the TOGA-COARE R/V *Natsushima* cruise. *J. Meteor. Soc. Japan*, **73**, 291–304, https://doi.org/10.2151/jmsj1965.73.2B_291.
- Zuidema, P., 1998: On the 600–800 mb minimum in tropical cloudiness observed during TOGA-COARE. *J. Atmos. Sci.*, **55**, 2220–2228, [https://doi.org/10.1175/1520-0469\(1998\)055<2220:TMMITC>2.0.CO;2](https://doi.org/10.1175/1520-0469(1998)055<2220:TMMITC>2.0.CO;2).